

Electronic Supporting Information

Low Magnetic Field Response Single-Phase Multiferroics under High Temperature

Jianlin Wang,^a Zhengping Fu,^{a,b,c} Ranran Peng,^{a,c} Min Liu,^{a,c} Shujie Sun,^a Haoliang Huang,^a Lin Li,^a Randy J. Knize^d and Yalin Lu^{a,b,c,d}*

^a CAS Key Laboratory of Materials for Energy Conversion, Department of Materials Science and Engineering, University of Science and Technology of China, Hefei 230026, P. R. China.

^b Hefei National Laboratory for Physical Sciences at the Microscale, University of Science and Technology of China, Hefei 230026, P. R. China.

^c Synergetic Innovation Center of Quantum Information & Quantum Physics, University of Science and Technology of China, Hefei 230026, P. R. China.

^d Laser and Optics Research Center, Department of Physics, United States Air Force Academy, Colorado 80840, USA.

* Correspondence E-mail: yllu@ustc.edu.cn.

SBFCT synthesis

To prepare the SrBi₅Fe_{0.5}Co_{0.5}Ti₄O₁₈ (SBFCT) sample, we followed the modified Pechini method (named as the citrate-nitrate combustion method). The specially designed two-step calcination route was used, which is schematically shown in Figure S1 and the details is described as following:

Both SrBi₄Ti₄O₁₅ (SBTi) and BiFe_{0.5}Co_{0.5}O₃ (BFCO-0.5) powders were synthesized using the combustion method. Excessive amounts of the raw materials were used to compensate the volatilization losses. Tetrabutyl titanate (C₁₆H₃₆O₄Ti) and nitrates (Sr(NO₃)₂, Bi(NO₃)₃·5H₂O, Fe(NO₃)₃·9H₂O, Co(NO₃)₂·6H₂O) were used as the starting materials, while citric monohydrate acid and ethylene diamine tetraacetic acid (EDTA) were taken as the coordinating agents. All reagents were analytically pure from Sinopharm Chemical Reagent Co., Ltd, CHN. Aqua fortis and aqueous ammonia was used to adjust the pH value to 6~7 and to form a stable transparent precursor solution. After being continuously stirred for 2 h, the solution was transferred to a ceramic dish and then was heated on a hotplate with a temperature of ~300°C. The solution underwent the processes of condensation, boiling and frothing to spillover. It was

hypergolic with a strong flame at last. The fluffy product was collected and calcined at 750°C for 3 h in an alumina crucible. The calcined products were grounded into powders in an agate mortar.

The mixture of SBTi and BFCO-0.5 powder was ball milled for 20 h by adding deionized water as dispersant. After ball milling, the slurry was dried at 80°C for 10 h and then was calcined at 800°C for 3 h. The calcined products were grounded into SBFCT powders. The obtained SBFCT powders were pressed into pellets. Then the pellets were sintered at 880°C, 10 MPa in an alumina die for 3 h in a hot press system (Materials Research Furnaces Inc., USA) with a processing gas (Ar/O₂=80/20). The hot pressed pellets were then sliced for various characterizations.

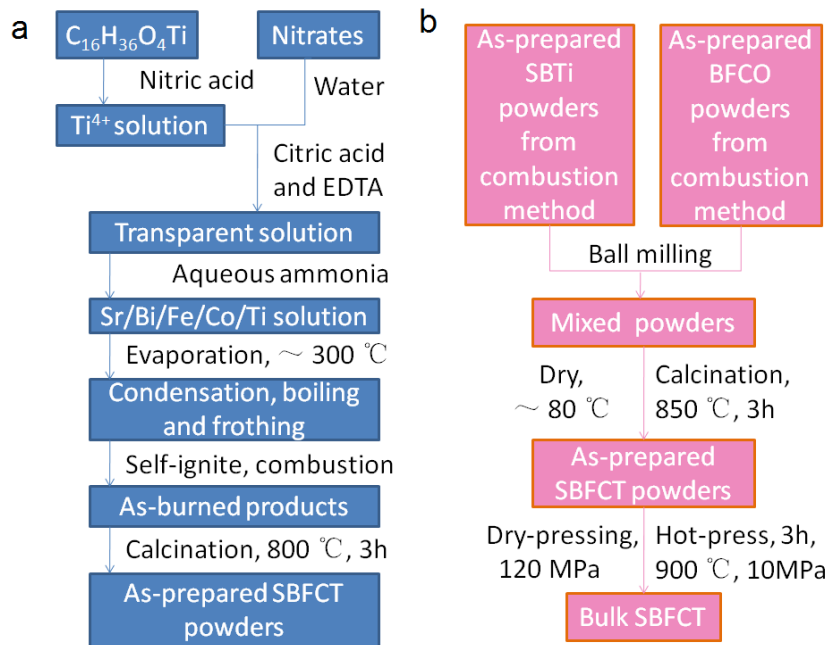


Figure S1. The flow chart of the specially designed route for synthesizing SBFCT. (a) The citrate-nitrate combustion method (using SrBi₄Ti₄O₁₅ (SBTi) as an example). (b) The two-step calcination route: SBTi and BiFe_{0.5}Co_{0.5}O₃ (BFCO-0.5) powders were ball milled and calcined to be SBFCT powders.

Characterizations

1. Powder X-ray Diffraction

Powders of the SBFCT sample were analyzed by the X-ray diffractometer (Rigaku TTR-III, Japan) in a Bragg angle range of 2θ (10°~60°) with the Cu Kα radiation (λ=1.5406 Å). XRD pattern of the SBFCT sample was refined using the Rietveld

method, corresponding to the five BO_6 octahedron slab layers in the Aurivillius structure. Here, we give a brief introduction to the Rietveld Method: ¹

The Rietveld's method requires a profile fitting, which is a least squares fit of a given and known profile function to the diffraction pattern by minimizing the function:

$$\phi = \sum_i w_i (y_i(\text{obs}) - y_i(\text{calc}))^2 = \text{Minimum} \quad (1)$$

y_i : the measured (and calculated) intensities at each step;

i : the summation index of all points in the diffraction pattern;

$w_i = 1/\sigma_i^2$: the weights given to each observation. σ_i : experimental error margins, which are assumed to be proportional to the square root of the count rate $y_i(\text{obs})$ following Poisson counting statistics.

Definition of R -indices used in Rietveld analyses:

$$R_p = \frac{\sum |y_i(\text{obs}) - (1/c)y_i(\text{calc})|}{\sum y_i(\text{obs})}$$

(2)

$$R_{wp} = \left[\frac{\sum w_i (y_i(\text{obs}) - (1/c)y_i(\text{calc}))^2}{\sum w_i (y_i(\text{obs}))^2} \right]^{1/2} \quad (3)$$

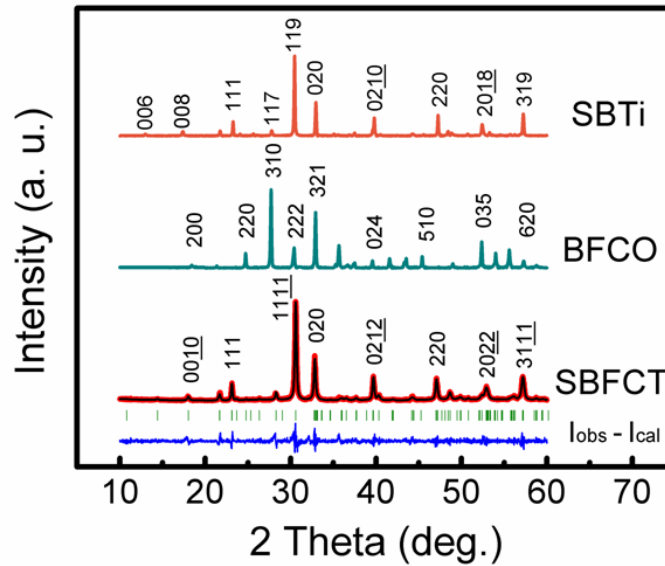


Figure S2. XRD patterns of the perovskite-type SBTi (orange), BFCO-0.5 (dark cyan), SBFCT (red) and the Rietveld refinement to the SBFCT results.

The XRD patterns of SBTi, BFCO-0.5 and SBFCT are given in Figure S2 correspondingly. It is found that all samples are single phase with no detectable secondary phases. The structural parameters of SBFCT sample are refined by using the Rietveld analyses. The refinements are started with the space group $F2mm$ with orthorhombic structure without deduction of the experimental background signal. The “goodness of fit” can be confirmed by the customarily calculated R -indices R_{wp} value of 13.32% and R_p value of 9.55%. The lattice parameters were $a=5.4626 \text{ \AA}$, $b=5.4517 \text{ \AA}$ and $c=49.184 \text{ \AA}$. SBFCT’s a and b parameters are slightly larger than those in SBTi ($a=5.445 \text{ \AA}$, $b=5.437 \text{ \AA}$),² which is due to that the effective ionic radii of Fe^{3+} (0.645 \AA) and Co^{3+} (0.61 \AA) are larger than that of Ti^{4+} (0.605 \AA) when they are six-fold coordinated by oxygen.³

2. Dielectric Properties

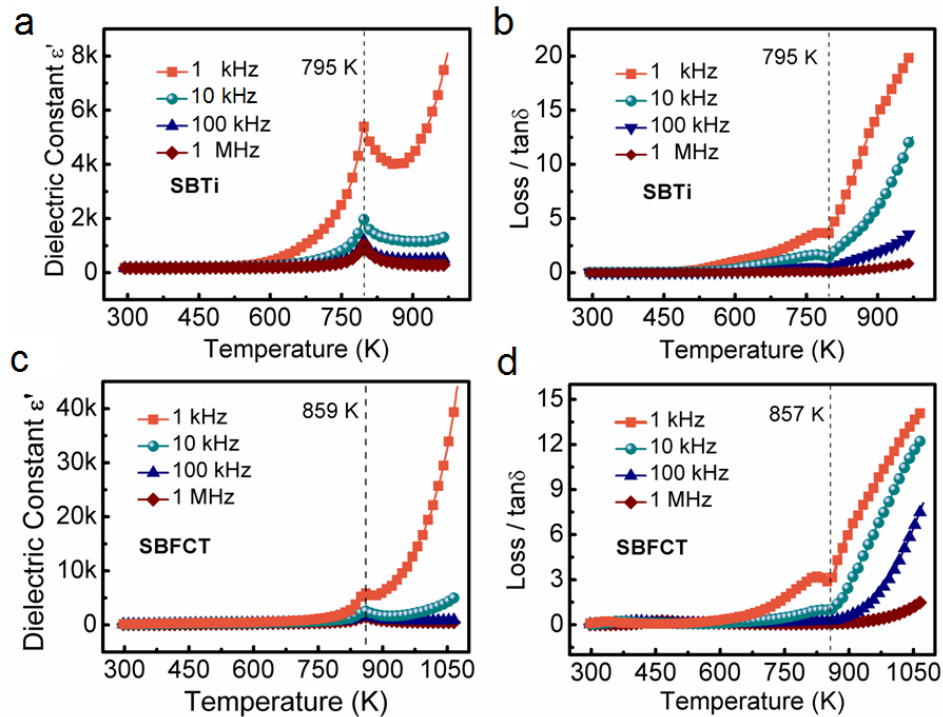


Figure S3. Temperature dependences of the dielectric permittivity and the dielectric loss in SBTi and SBFCT ceramics at different test frequency: 1, 10, 100 and 1000 kHz. (a) Temperature dependence of the dielectric constant in SBTi. (b) Temperature dependence of the dielectric loss in SBTi. (c) Temperature dependence of the dielectric constant in SBFCT. (d) Temperature dependence of the dielectric loss in SBFCT.

Temperature dependences of the dielectric permittivity and the dielectric loss were recorded using an in-house dielectric measurement setup. SBTi and SBFCT ceramics were made into pellets with a diameter of 12 mm and a thickness of 0.5 mm. Both sample sides were covered with platinum pastes and were heated at 800°C for 2h in order to achieve a good electrical contact. Temperature dependences of the dielectric constant and the loss results are given in Figure S3. From the Figure S3a and b, the transition temperature (Curie temperature, T_c) of SBTi is 795 K, which matches well with the reported results.^{2,4} Figure S3c shows the temperature dependence of the dielectric constant in SBFCT, indicating that the T_c is 859K, which is much higher than that of SBTi. Figure S3d shows the temperature dependence of the dielectric loss in SBFCT, indicating a very close T_c of 857 K. The increased dielectric loss at high temperature is assumed to be caused by the increase in conductivity.

3. Magnetic Properties

The room temperature magnetic properties of SBTi and BFCO-0.5 samples were recorded on the SQUID-VSM (Quantum Design Inc., USA), and the results are shown in Figure S4. According to the relationship of magnetization versus magnetic field, SBTi was determined to be diamagnetic, while BFCO-0.5 is ferromagnetic with $M_r = 1.08$ emu/g and $H_c = 156$ Oe. SBFCT shows a room temperature ferromagnetic hysteresis loop with $M_s = 5$ emu/g, and the bottom-right inset indicates $M_r = 1.12$ emu/g and $H_c = 116$ Oe.

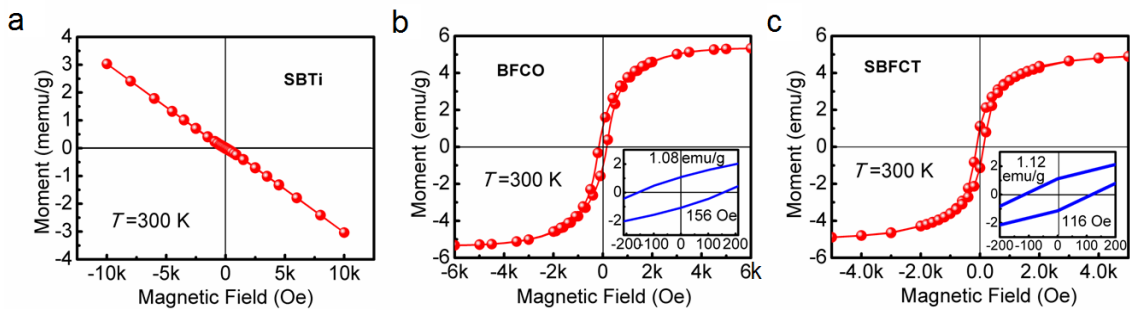


Figure S4. Room temperature magnetic properties of $\text{SrBi}_4\text{Ti}_4\text{O}_{15}$ (SBTi), $\text{BiFe}_{0.5}\text{Co}_{0.5}\text{O}_3$ (BFCO-0.5) and $\text{SrBi}_5\text{Fe}_{0.5}\text{Co}_{0.5}\text{Ti}_4\text{O}_{18}$ (SBFCT). (a) Magnetic field dependence of magnetization of SBTi. (b) Magnetic field dependence of magnetization of BFCO-0.5. (c) Magnetization versus magnetic field strength (M - H) loop of the SBFCT at the RT.

4. X-ray Photoelectron Spectroscopy (XPS) Measurement

The X-ray photoelectron spectroscopy (XPS) measurement was done using a Thermo Scientific ESCALAB 250Xi XPS instrument with a monochromatic Al K α X-ray source and a background pressure in the analysis chamber of 10^{-9} – 10^{-10} mbar. The nominal energy resolution and spatial resolution were of 0.45 eV and 20 μm , respectively. Data were collected and analyzed using the adventitious C 1s peak with a fixed value of 284.8 eV.

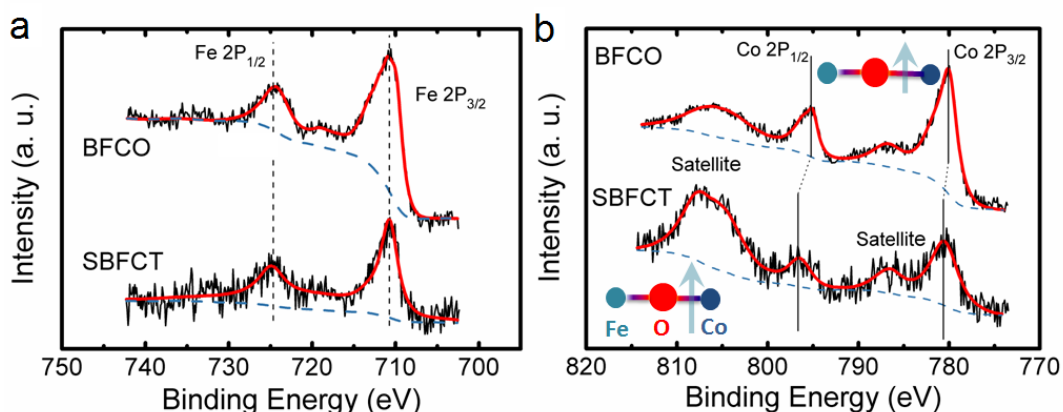


Figure S5. XPS spectra of (a) Fe 2p and (b) Co 2p core-level for both BFCO-0.5 and SBFCT samples.

Figure S5 shows the X-ray photoemission spectroscopy (XPS) spectra of Fe 2p and Co 2p core-levels in both BFCO-0.5 and SBFCT samples. The binding energy peak of the Fe 2p_{3/2} locates at 710.78 eV for both BFCO-0.5 and SBFCT (dashed lines in Figure S5a, also see Table S1), which are in coincidence well to that in Fe₂O₃ (710.8 eV),⁵ indicating that Fe ions in BFCO-0.5 and SBFCT may favor the trivalent state. Broadness of the 2p core-level peaks can be attributed to electrostatic interactions, spin-orbit coupling between the 2p core hole and unpaired 3d electrons of the photoionized Fe cation and the surrounding crystal field interactions.⁶ From the Fe 2p core-level spectra, very weak intensity of satellite peak can be observed with an energy separation of $\Delta E_{(\text{satellite-Fe } 2P_{3/2}\text{main peak})}$ very close to 8.5 eV, which means the high spin state of Fe³⁺ coordinated by oxygen anions.⁵ Figure S5b shows the Co 2p core-level spectra of both BFCO-0.5 and SBFCT. Intense satellite peaks of Co 2p spectra can be observed in both BFCO-0.5 and SBFCT too. Strong satellite peaks⁷ of Co 2p strongly support that Co

cation stay as the high-spin Co^{2+} , rather than the diamagnetic Co^{3+} ion or the low-spin Co^{2+} . The phenomenon that satellite peaks accompanied by the Co 2p main lines can be attributed to the “electron shake-up” effect, in a multi-electron excitation mechanism. Figure S5b shows that the peak value is 780.07 eV for BFCO-0.5 and 780.64 eV for SBFCT, which matches well to that in CoO (780.0 eV), indicating a divalent state with high-spin. When BFCO-0.5 was incorporated into SBTi to form SBFCT, the cobalt valence increases but not completely oxidized to the trivalent state (781.3 eV of Co $2p_{3/2}$ in SBFCT). Interestingly, with increasing the cobalt ion valence, the shake-up excited satellite peaks seem to be stronger. This is consistent with the higher spontaneous magnetic moment per Fe-O-Co chain from the RT saturated magnetization of the M-H hysteresis for BFCO-0.5 and SBFCT. This effect is illustrated in Figure S5b as Fe-O bond stays constant and Co-O bond increases its interaction strength, resulting in an increase in the total magnetic moment.

Table S1. XPS binding energy of 2p core-level spectra for sample BFCO-0.5 and SBFCT

Sample	Fe 2p Core-Level (BE, eV)			Co $2p_{3/2}$ (BE, eV)			Co $2p_{1/2}$ (BE, eV)			
	$2p_{3/2}$ MP ^a	$2p_{1/2}$ MP	Δ_{S-L} ^b	MP	SP ^c	ΔE ^d	MP	SP	ΔE	Δ_{S-L}
BFCO-0.5	710.78	724.48	13.7	780.07	786.84	6.77	795.20	806.27	11.07	15.13
SBFCT	710.78	724.88	14.1	780.64	786.70	6.06	796.92	807.53	10.61	16.28

^a MP, binding energy of the main peak; ^b Δ_{S-L} , spin-orbit splitting energy; ^c SP, binding energy of the satellite peak, ^d ΔE , energy separation between the main peak and satellite peak.

5. Magnetic Thermogravimetric Analysis (MTGA)

The magnetic thermogravimetric analysis (MTGA)⁸ is accurate and sensitive to the magnetic impurity’s existence, which was performed to determine ferromagnetic Curie transition temperature (T_{CM}) using the instrument TGA Q5000 (TA Instruments, United States). We have used the mixture of well recognized ferromagnetic material CoFe_2O_4 and non-magnetic material ZrO_2 as the test standard to explore the detection sensitivity. From Figure S6a, we have found that the magnetism from the sample with a 0.5 wt.% CoFe_2O_4 mixture is still detectable, which determines that the MTGA method is highly sensitive to detect the magnetic impurities. The results indicate that the sample does not contain other magnetic impurities under the MTGA’s detectivity.

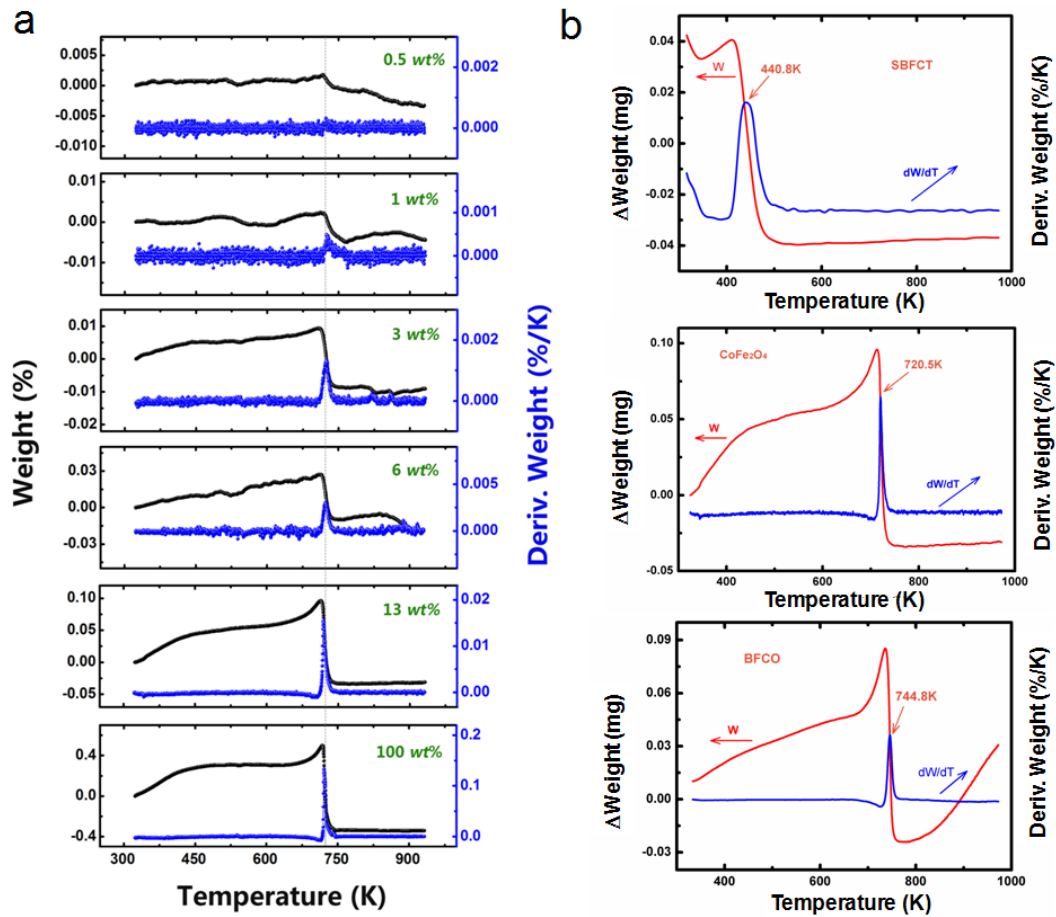


Figure S6. Magnetic thermogravimetric analysis (MTGA) for the determination of magnetic Curie temperature: (a) a mixture of CoFe_2O_4 and ZrO_2 ; (b) SBFCT, CoFe_2O_4 , and BFCO-0.5.

6. Ferroelectric Properties

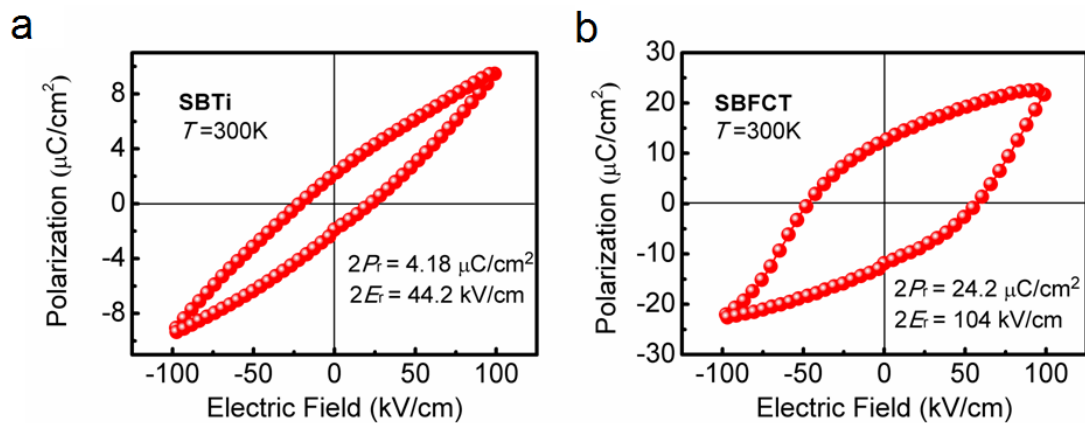


Figure S7. Ferroelectric properties of SBTi and SBFCT at the room temperature. (a) Hysteresis loop of SBTi at the 100 kV/cm test electric field. (b) Hysteresis loop of SBFCT at the 100 kV/cm test electric field.

Ferroelectric hysteresis loops were recorded by the Precision Multiferroic Precision Material Analyzer (Radiant Technologies, USA). Because that the SBTi will be electrically breakdown if the test electric field is above 100 kV/cm at the room temperature, so we compare the ferroelectric properties below an electric field of 100 kV/cm. The results were shown in Figure S7. According to the hysteresis loop, we can determine the $2P_r$ value of $4.18 \mu\text{C}/\text{cm}^2$ and the $2E_c$ value of 44.2 kV/cm for SBTi, while those values for SBFCT are $24.2 \mu\text{C}/\text{cm}^2$ and 104 kV/cm, respectively. It is clear that a tremendous enhancement of the ferroelectric property has been achieved by inserting the magnetic layer into the Aurivillius SBTi, which may be caused by a large off-center distortion inside the perovskite layers.

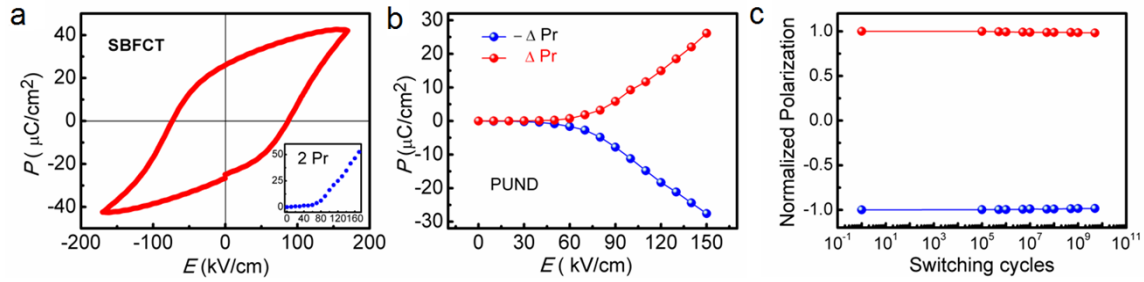


Figure S8. Ferroelectric properties of SBFCT at the room temperature. (a) P - E hysteresis loop of SBFCT at the 170 kV/cm test electric field. (b) Plot of $\pm \Delta P_r$ versus the testing electric field in a standard PUND measurement. (c) Normalized polarization in the fatigue test.

Figure S8a shows the ferroelectric property of SBFCT bulk sample at RT. The polarization versus electric field (P - E) hysteresis loop shows a remanent polarization ($2P_r$) of $52.4 \mu\text{C}/\text{cm}^2$ and a coercive electric field ($2E_c$) value of 160 kV/cm at the testing electric field of 170 kV/cm. The Standard positive-up-negative-down (PUND) measurement was introduced to characterize if there is any artificial polarization from the leakage (results shown in Figure S8b). The measured switched polarization value (ΔP_r) is consistent well with the $2P_r$ obtained from the customary ferroelectric loop (see the bottom-right inset in Figure S8a). Polarization fatigue was measured at the frequency of 1 KHz and with an electric field of 150 kV. Figure S8c shows that the degradation of the polarization is negligible after 10^9 switch cycles.

7. Resistivity

Temperature dependant resistivity of the SBFCT sample was measured with two-probe method. Due to its high resistivity at low temperatures, we could only measure the DC electric property at the starting temperature of $\sim 503\text{K}$ and then above. According to the negative temperature coefficient (NTC) which has been widely accepted in most semiconductors in a certain temperature range, we use the formula ($\rho = \alpha \cdot e^{\frac{\beta}{T}}$) to extrapolate the sample's resistivity to the room temperature (Figure S9).

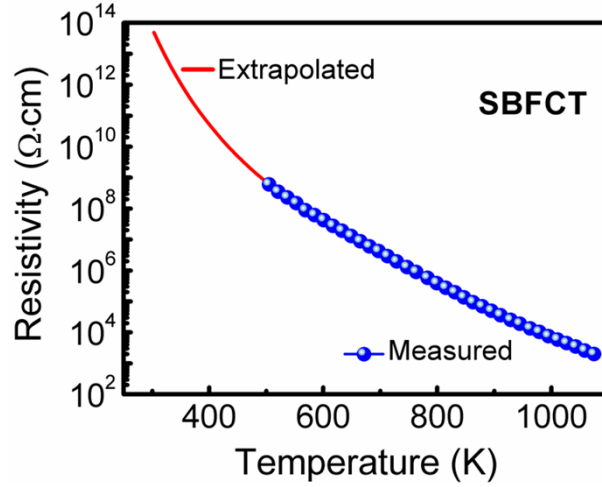


Figure S9. The temperature dependant resistivity of the SBFCT sample. The blue ball line indicates measured data and the red line indicates the extrapolated data.

8. Magneto-Capacitance (MC) Effect Measurement Method

The magneto-capacitance (MC, or magneto-dielectric) method has been widely used as an indirect measurement to evidence the magneto-electric (ME) coupling. The measured results were shown inside the main article. From the view of Ginzburg-Landau theory and the approximation under the condition of $T_M \ll T_E$ (T_M : magnetic ordering temperature, T_E : electric ordering temperature), the thermodynamic potential Φ can be written in the form:

$$\Phi = \Phi_0 + \alpha P^2 + \frac{\beta}{2} P^4 - PE + \alpha' M^2 + \frac{\beta'}{2} M^4 - MH + \gamma P^2 M^2 \quad (4)$$

where P and M are the polarization and the magnetization, respectively. Φ , α , β , α' , β' , and γ are functions of the temperature.

Difference of the relative dielectric constant can then be semi-quantitatively defined as follow:

$$\delta\varepsilon \propto \gamma M^2 \quad (5)$$

To quantify the magneto-dielectric effect, a Maxwell-Wagner (M-W) capacitor model system, which consists of two leaky capacitors in series (Figure S10a), was used in simulations. The real and imaginary parts of its permittivity are given as follows,⁹

$$\varepsilon'(\omega) = \frac{1}{C_0(R_i + R_b)} \frac{\tau_i + \tau_b - \tau + \omega^2 \tau_i \tau_b \tau}{1 + \omega^2 \tau^2} \quad (6)$$

$$\varepsilon''(\omega) = \frac{1}{\omega C_0(R_i + R_b)} \frac{1 - \omega^2 \tau_i \tau_b + \omega^2 \tau(\tau_i + \tau_b)}{1 + \omega^2 \tau^2} \quad (7)$$

where subindex i and b refer to the interfacial-like and bulk-like layers, respectively,

$$\tau_i = C_i R_i, \quad \tau_b = C_b R_b, \quad \tau = \frac{\tau_i R_b + \tau_b R_i}{R_i + R_b}, \quad C_0 = \varepsilon_0 \frac{A}{t},$$

A is the area of the capacitor, and t is the thickness.

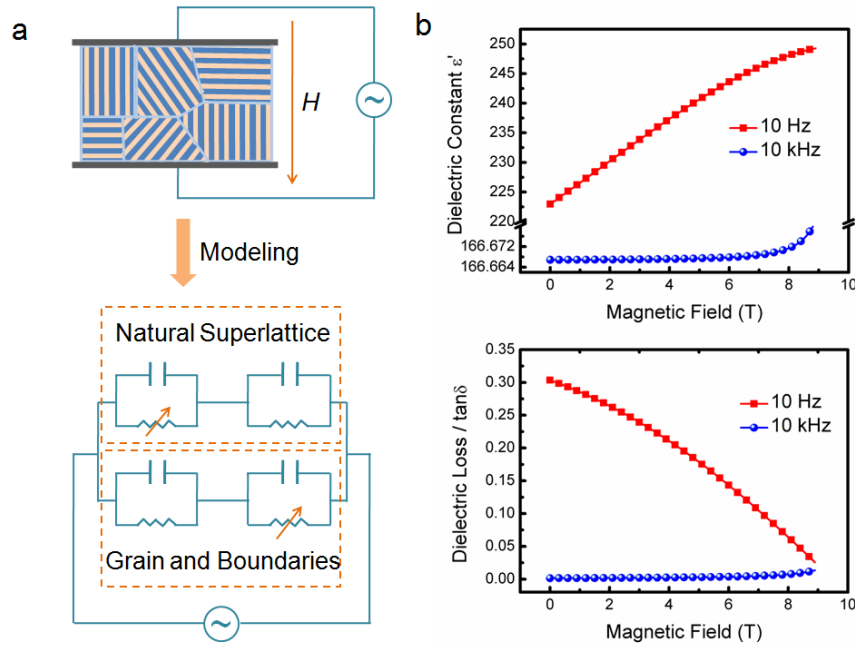


Figure S10. Magneto-dielectric modeling. (a) Schematic of the capacitor system (grains separated by light blue boundaries and the interlayer strips of orange and blue indicating the superlattice inside the grains) and its leaky capacitor modeling. (b) The results of the simulation.

Taking equation (6) and (7), and performing the general substitutions of $R_i = \rho_i t_i / A$, $R_b = \rho_b t_b / A$, $C_i = \varepsilon_i A / t_i$, $C_b = \varepsilon_b A / t_b$, and $t = t_i + t_b$. In these equations, the absolute thickness is actually irrelevant, and what really matters is the thickness ratio t_i / t_b . If considering the fact that the number of interfaces between bismuth oxide layer and perovskite layer within the grain is much more than the grain boundaries, we could assume that the superlattice effect will dominate the magneto-dielectric effect. Here, the interfacial layer is the bismuth oxide layer and the bulk-like layer is the perovskite layer. The relative dielectric constants of these two layers are assumed to be $\varepsilon_r \sim 50$ for the bismuth insulating layer and $\varepsilon_r \sim 500$ for the perovskite layer.² The resistivity of the perovskite is assumed to be $10^8 \Omega \cdot \text{cm}$ and has a linear negative magneto-resistance, with the bismuth oxide layer having a resistivity 4 orders higher and $t_i / t_b = 0.2$. The calculated results for $\omega = 10 \text{ Hz}$ and 10 kHz are given in Figure S10B.

9. The Dynamic Magneto-electric (ME) Effect Measurement Method ¹⁰

In the dynamic method, the ME signals induced by an oscillating magnetic field can be measured at different DC magnetic fields using the lock-in modulation technique. The ME measuring system mainly consists of a DC electromagnet, an AC Helmholtz coil, a lock-in amplifier and a gaussmeter. When an AC field is superimposed over a tunable DC electromagnet, the effective field is

$$H = H_0 + h_0 \sin(\omega t)$$

(8)

The magnetic induced ME output voltage (V) can be approximated as a second-order effect as follow:

$$V \propto (\alpha H + \beta H^2)$$

(9)

where α and β are the coefficients of linear and quadratic components of the ME effect. With the lock-in amplifier, we can measure the ME output signal at a fixed frequency ω

$$V \propto (\alpha + \beta H_0) h_0 = \alpha^* (H_0) h_0$$

(10)

$\alpha^*(H_0)$ is a pseudo-linear coefficient related to the DC field H_0 . If we take the sample thickness (t) into account, we can obtain the dynamic ME coupling coefficient in the form of

$$\alpha_{\text{ME}} = \frac{\alpha^*(H_0)}{t} = \frac{1}{t} \times \frac{V}{h_0} \quad (11)$$

References

- 1 G. Will, *Powder Diffraction: The Rietveld Method and the Two-Stage Method*, Springer, Berlin, GER 2006.
- 2 H. Irie and M. Miyayama, *Appl. Phys. Lett.* 2001, **79**, 251.
- 3 R. D. Shannon, *Acta. Cryst.* 1976, **A32**, 751.
- 4 A. R. James, G. S. Kumar, T. Bhimasankaram and S. V. Suryanarayana, *Bull. Mater. Sci.* 1994, **17**, 951.
- 5 A. P. Grosvenor, B. A. Kobe, M. C. Biesinger and N. S. McIntyre, *Surf. Interface Anal.* 2004, **36**, 1564.
- 6 R. P. Gupta and S. K. Sen, *Phys. Rev. B* 1974, **10**, 71.
- 7 B. J. Tan, K. J. Klabunde and P. M. A. Sherwood, *J. Am. Chem. Soc.* 1991, **113**, 855.
- 8 R. L. Blaine and P. G. Fair, *Thermochimica Acta* 1983, **67**, 233.
- 9 H. M. Jang, J. H. Park, S. Ryu and S. R. Shannigrahi, *Appl. Phys. Lett.* 2008, **93**, 252904.
- 10 M. M. Kumar, A. srinivas, S. V. Suryanarayana, G. S. Kumar and T. Bhimasankaram, *Bull. Mater. Sci.* 1998, **21**, 251.